

# Wide bandgap semiconductor nanomembranes as a long-term bio-interface for flexible, implanted neuromodulator

**Tuan-Khoa Nguyen**

Griffith University

**Matthew Barton**

Griffith University

**Aditya Ashok**

The University of Queensland <https://orcid.org/0000-0003-0479-0348>

**Thanh-An Truong**

Griffith University

**Sharda Yadav**

Griffith University

**Michael Leitch**

Griffith University

**Thanh-Vinh Nguyen**

AIST

**Navid Kashaninejad**

Griffith University

**Toan Dinh**

University of Southern Queensland

**Leonie Hold**

Griffith University

**Yusuke Yamauchi**

The University of Queensland <https://orcid.org/0000-0001-7854-927X>

**Nam-Trung Nguyen**

Griffith University <https://orcid.org/0000-0003-3626-5361>

**Hoang-Phuong Phan** (✉ [h.phan@griffith.edu.au](mailto:h.phan@griffith.edu.au))

Griffith University

---

**Article**

**Keywords:**

**Posted Date:** January 28th, 2022

**DOI:** <https://doi.org/10.21203/rs.3.rs-1305833/v1>

**License:**  This work is licensed under a Creative Commons Attribution 4.0 International License.

[Read Full License](#)

---

# **Wide bandgap semiconductor nanomembranes as a long-term bio-interface for flexible, implanted neuromodulator**

*Tuan Khoa Nguyen,<sup>1</sup> Matthew Barton,<sup>2</sup> Aditya Ashok,<sup>1,3</sup> Thanh-An Truong,<sup>1</sup> Sharda Yadav,<sup>1</sup> Michael Leitch,<sup>2</sup> Thanh-Vinh Nguyen,<sup>4</sup> Navid Kashaninejad,<sup>1</sup> Toan Dinh,<sup>5</sup> Leonie Hold,<sup>1</sup> Yusuke Yamauchi,<sup>3</sup> Nam-Trung Nguyen,<sup>1</sup> Hoang-Phuong Phan<sup>\*,1</sup>*

<sup>1</sup> Queensland Micro and Nanotechnology Centre, Griffith University, QLD, Australia

<sup>2</sup> School of Nursing and Midwifery, Griffith University, QLD, Australia

<sup>3</sup> Australian Institute for Bioengineering and Nanotechnology, The University of Queensland, Queensland 4072, Australia

<sup>4</sup> The National Institute of Advanced Industrial Science and Technology (AIST), Tsukuba, Japan

<sup>5</sup> Centre for Future Materials, University of Southern Queensland, Queensland 4305, Australia

Email: [h.phan@griffith.edu.au](mailto:h.phan@griffith.edu.au)

Keywords: Implanted electronics, neuromodulation, long-lived biobarrier, flexible electronics, wide bandgap semiconductors, nanomembranes

## **Abstract**

Electrical neuron stimulation holds promise for the treatment of several chronic neurological disorders, including spinal cord injury, epilepsy, and Parkinson's disease. The implementation of ultrathin, flexible electrodes, that can offer non-invasive attachment to soft neural tissues, is a breakthrough technology for timely, continuous, programable, and spatial stimulations. However, to enable flexibility in neural electrodes, the conventional thick and bulky ceramic package is no longer applicable to soft electronics, which poses several technical issues such as device degradation and long-term stability. We introduce herein a new concept of long-lived flexible neural electrodes using silicon carbide nanomembranes as the Faradaic interface, and thermal oxide thin films as the electrical isolation layer. The silicon carbide (SiC) membranes were developed using a wafer-level chemical deposition process while thermal oxide was grown employing a standard and high-quality wet oxidation approach, which are scalable and compatible with industrial microelectronic technologies. Our experimental results showed excellent stability in the SiC/SiO<sub>2</sub> hybrid system that can potentially last several decades with maintained reliable electrical properties in biofluid environments. We demonstrated the capability of our material system in stimulating peripheral nerves (i.e., sciatic nerve) in rat models, showing comparable muscle contraction response recorded from electromyogram (EMG) stimulation results to a gold-standard non-implanted nerve stimulation device. The design concept, scalable fabrication approach, and the multimodal functionalities in SiC/SiO<sub>2</sub> flexible electronics open an exciting possibility for fundamental neuroscience studies as well as clinical neural stimulation-based therapy.

## Introduction

Neurological disorders such as Parkinson's disease, traumatic brain injuries, and spinal cord injuries are the leading causes of the disability-adjusted life-year and low probability of recovery<sup>1, 2</sup>. Biomedical innovations that can enhance the restoration and regeneration of dysfunctions caused by neurological injuries have attracted a great deal of interest for improving the quality of life for patients and bringing economic benefit to the society. Implanted neuromodulation devices are one of the key technologies for the diagnosis and treatment of neurological disorders<sup>3, 4, 5, 6</sup>. For instance, deep brain stimulators have been widely deployed for the treatment of Parkinson's disease where electrical stimuli produced from implanted electrodes can help in regulating dysfunctional brain regions<sup>7, 8</sup>. Vagus nerve stimulators that send electrical impulses along the nerve to the brainstem have been approved by the Food and Drug Administration (FDA) for their proven efficacy in managing epilepsy in patients who do not adequately respond to anti-seizure medications<sup>9</sup>. Recent progress in neuromodulation therapy through the electrical excitation of peripheral nervous systems (PNS) suggests promising paths for the restoration of motor neurons and the subsequent reactivation of targeted muscle contraction to produce movement of paralyzed limbs in patients with spinal cord injuries<sup>10, 11</sup>.

Successful outcomes in preclinical trials demonstrated over the last decade have facilitated the development and innovation of advanced bioimplantable electronics for neuron stimulation<sup>12, 13, 14, 15</sup>. The two mainstream neuromodulation systems are (i) intraneural electrodes which can penetrate deeply into the neural tissues and (ii) extraneural electrodes which afford a conformal contact with the curvilinear surface of neural tissue. Intraneural devices, such as the Utah slanted electrode arrays, have several advantages such as a close proximity to the target nerve, and the capability to activate nerve fascicles individually<sup>16</sup>. In many cases, the extraneural approach is preferred due to the lower risk of nerve damage and potentially higher resolution for spatial physiological mapping<sup>17</sup>. Flexible electronics are considered the

backbone technology for the realization of modern extraneural stimulators, in which the integration of soft semiconductors, ultrathin metallic interconnectors, and polymeric substrates offer ideal mechanical matching between functional devices and tissue<sup>6, 13, 14, 18</sup>. Several types of distributed arrays of electrodes on soft substrates combined with wireless communication modules such as near field communication (NFC) have shown potential for the monitoring and treatment of several neural disorders<sup>19, 20</sup>. Due to the minimal thickness of all constructing elements to enable mechanical flexibility, most available material systems for soft electronics only last for a short period of time inside the human body as a result of hydrolysis reaction<sup>21</sup>. This *in situ* chemical-based phenomenon has been utilized for degradable devices, where the implanted components can be safely dissolved when they are no longer needed<sup>8, 21</sup>. However, for many chronic diseases, implanted flexible electronics that can last over several decades or even a patient's lifetime are imperative<sup>22, 23</sup>. The shortfall in the material library of robust, electrically insulating biobarriers and functional biointerfaces for prolonged uses raises the demand for thin-film materials that can simultaneously provide mechanical deformability and reliable operation in biofluids for a long lifespan<sup>24</sup>. Several studies demonstrated fully covered thermal oxide nanomembranes as a biobarrier in a capacitive coupling interface for continuous cardiovascular electrophysiological mapping<sup>25</sup>. Nevertheless, these platforms were unable to offer direct electronics-tissue interfaces limiting their potential in extracellular stimulation. Another work used TiSi<sub>2</sub> nanothin films as the Faradaic interface and the biobarrier layer, which can circumvent the limitation in capacitive interfaces; however, they inherit the limited functionalities of metallic based materials<sup>26</sup>. In addition, the effectiveness of these materials on animal models or preclinical studies has yet to be validated. A long-term stable semiconductor-biotissue interface at targeted areas is still demanded to enable potential capabilities such as photoelectrochemical modulation, mechanotransduction, thermal sensing, and neuronal stimulation.

This paper presents a bioelectronic platform incorporating SiC and SiO<sub>2</sub> nanomembranes hybrid structure as the biointerface and biobarrier that can deliver reliable long-term operations for bioimplanted applications. Our fabrication technologies employ industrially compatible processes to form SiC/SiO<sub>2</sub> films using wet thermal oxidation, taking advantage of the chemical inertness of SiC material at elevated temperatures. Experimental results demonstrate excellent mechanical flexibility in the SiC electronics along with long-term stability in simulated biofluid environments. *In vivo* animal studies provide proof of concept for the potential use of our material system for peripheral nerve excitation and the generation of muscle contraction. Our technology opens promising possibilities towards long-term stable and multimodal flexible electronics for neuromodulation applications.

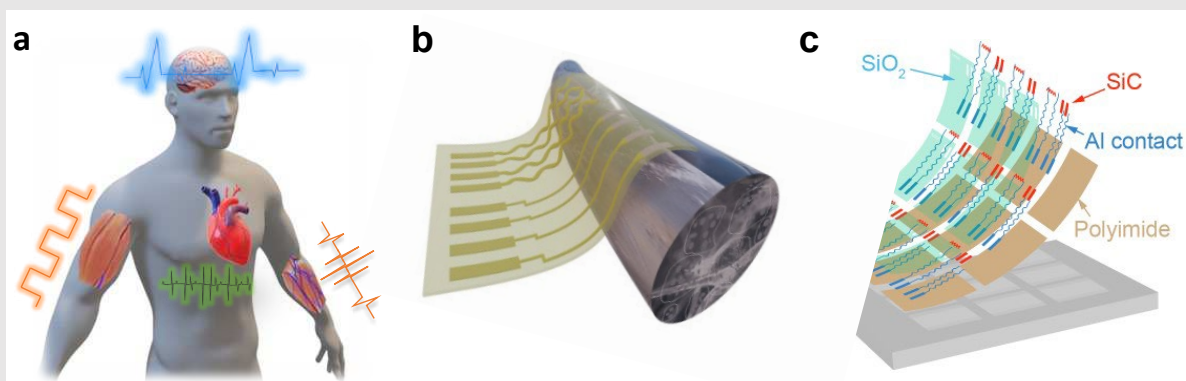


**Figure 1** SiC electronics for nerve stimulation protocol: a) Concept of SiC/SiO<sub>2</sub> implanted electronics for neuromodulation for the recovery of motor and physiological functions. b) Schematic illustration of the flexible SiC/SiO<sub>2</sub> wrapped around a nerve for long-term electrical stimulation and sensing. c) Exploded view of SiC/SiO<sub>2</sub> electronic system for long-lived implanted electronics.

## Results

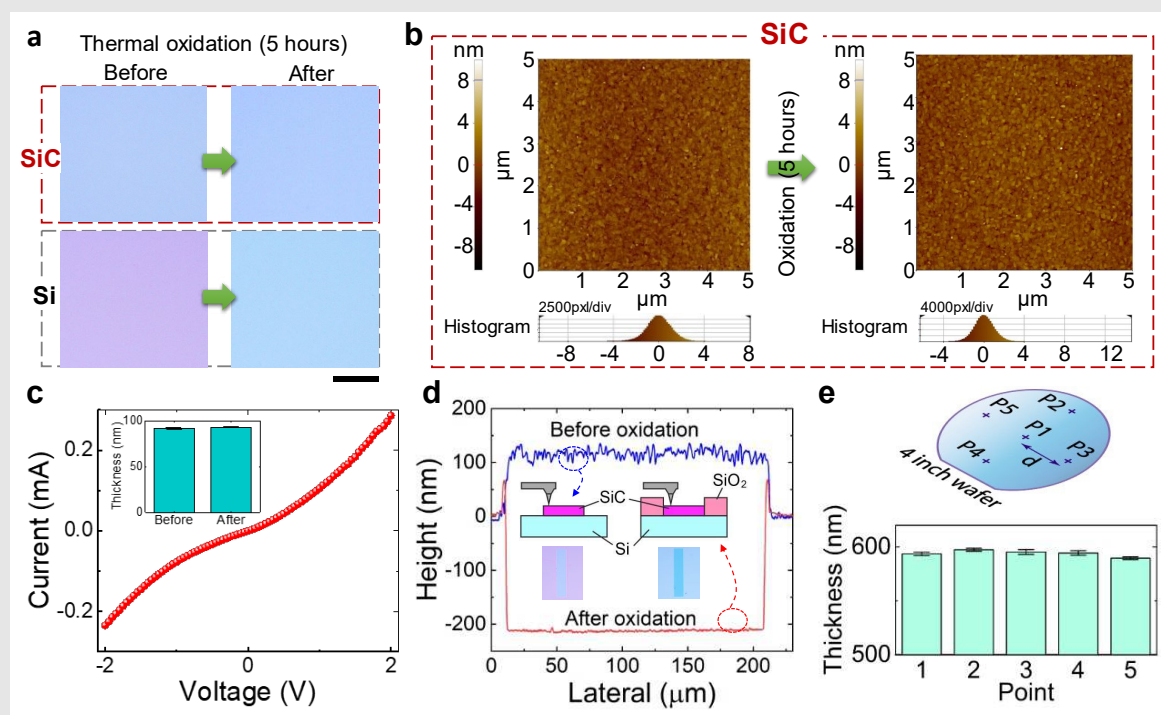
### *Concept of SiC implantable electronics for nerve stimulation.*

Figure 1(a) shows the conceptual neuromodulation of long-lived bioimplanted SiC electronics to recover critical communication between central nervous systems and

neuromuscular junctions. The system, via electronics/nerve interfaces, has potential for long-term, therapeutic modality for restoration of chronic motor-based disorders, such as muscle/nerve stimulations for peripheral nerve regeneration and vagal modulations for treatments of heart conditions (hypertension and heart failure)<sup>27</sup>, epileptic seizure<sup>28</sup>, and depression<sup>29</sup>. An ideal platform would provide well-matched mechanical properties with soft tissue together with the capabilities of offering electrochemical functions for Faradaic interface to deliver useful neuron stimulation and/or recording, Figure 1(b). Advanced implanted bioelectronic systems are also expected to offer integrated biophysical sensing function to monitor real-time biosignal data. Figure 1(c) shows the layered-structure of long-lived implantable SiC bioelectronics where highly-doped SiC provides a direct electrical interface (i.e., Faradaic interface) with neural tissue, while the thin thermal oxide membrane functions as a long-term stable insulation/biobarrier. As well as their excellent tolerance to hydrolysis, both SiC and thermal oxide exhibit good dielectric constant (9.72 for SiC, and 3.70 for SiO<sub>2</sub>) and optical transparency (over 70% in 200nm-thick SiC and nearly 100% in 600nm-thick SiO<sub>2</sub> in the visible wavelengths), suggesting the promising possibility for implanted optoelectronics applications. Metal traces interconnects to the SiC electrodes were formed by conventional cleanroom processes (i.e., sputtering and wet etching, see Method sections) to create interconnects for the SiC electrodes. A thin polyimide film with a thickness of approx. 10 μm was spin-coated and utilized as the soft substrate of the implanted devices. The removal of the initial Si hosting wafer using a combination of deep reactive ion etching (DRIE) and xenon difluoride (XeF<sub>2</sub>) dry etching leaves a SiC/SiO<sub>2</sub> hybrid structures on a polyimide substrate. Due to the extremely low bending stiffness in the ultrathin SiC and thermal oxide nanomembranes along with the intrinsic mechanical flexibility of the polyimide film, our platform can offer conformal contact with neural tissue, primarily enabling the SiC electrodes to wrap around peripheral nerves for electrical stimulation. Electrical stimulation of peripheral nerves (e.g., sciatic nerve in a rat model in this work) is expected to evoke corresponding muscle activity,

suggesting a promising pathway to regain limb-control in patients with spinal cord injuries. A detailed description of the fabrication approach and material processing can be found in the Methods section and Supplementary Notes 1 & 2 and Figure S2.

### Formation of the SiC and SiO<sub>2</sub> hybrid structure



**Figure 2.** Characterization of silicon oxide on SiC utilizing a CMOS (complementary metal-oxide-semiconductor) compatible thermal oxidation process: a) colorimetric observation under optical microscopy: no color change observed for SiC after oxidation for 5 hours whilst Si color clearly changed, scale bar, 100 $\mu$ m. b) Atomic force microscopy inspection of surface morphology of SiC before and after the oxidation process. c) Current-voltage characteristics of SiC after oxidation, inset: thickness of SiC before and after oxidation d) Step height change after oxidation for SiC patterned samples. e) Uniformity of SiO<sub>2</sub> thickness across 6 inch SiC-on-Si wafer after oxidation.

Nanorh SiC films were deposited on a Si substrate using a chemical vapor deposition process inside a hot wall chamber at a low pressure<sup>30, 31</sup>. Details of the characterization of 3C-SiC can be found in our previous studies, which showed the film as single crystal (using SAED

measurement) with crystallography orientation along the (100) direction (using XRD measurement)<sup>32</sup>. SiC electrodes were patterned using standard photolithography and ICP etching (see Methods section). The exposed Si areas were then oxidized inside a controlled humidity chamber at 900°C for a duration of 5 hours, Figure 2. The excellent oxidation-tolerance of SiC is well reflected by colorimetric observation under optical microscopy (Olympus<sup>TM</sup> MX50AF-IC); whereas Si reacted with vaporized water molecules ( $Si + H_2O \rightarrow SiO_2 + 2H_2$ ) and turned its color from purple to light blue as shown in Figure 2(a). The surface morphology and roughness of the SiC layer before and after oxidation were characterized by an Atomic Force Microscope (i.e., Park AFM<sup>TM</sup> NX20), showing no significant change (approximately 2nm root mean square (RMS)), which indicates the stability of SiC at high temperature and wet oxidation conditions, Figure 2(b). The thicknesses of SiC film before and after oxidation were quantified using a thin film measurement (i.e., Nanometrics<sup>TM</sup> AFT 210), showing a similar value of 93nm. Since there was almost no oxide layer formed on SiC, we can clearly observe a high current density in the SiC electrodes by directly placing metal probes on the SiC surface after thermal oxidation without the requirement for hydrofluoric acid (HF) treatment, Figure 2(c). This result clearly emphasizes the excellent electrical property of SiC for Faradaic interfaces under high oxidation conditions including biofluid environments. Based on the optical thin-film measurement, we observed an oxide layer with a thickness of approx. 590nm grown on the exposed Si area. To further estimate the amount of the consumed Si layer, we employed a depth profile scan (i.e., Dektak<sup>TM</sup> 150) to measure the changes in step heights of the deposited films, Figure 2(d). The thickness of the consumed Si layer was calculated as:  $t_{Si} = t_{SiO_2} - (t_{before} + t_{after})$ , and was found to be 240nm (see Supplementary Note 3 and Figure S3). Accordingly, the ratio between the thickness of the consumed Si layer (240nm) and that of the as-grown thermal oxide (580nm) is 0.43:1 (i.e., 240nm/580nm), consistent with Deal and Grove's oxidation model for the crystalline silicon in (100) orientation (i.e., 0.44:1)<sup>33</sup>. The as-grown thermal oxide layer exhibits an excellent uniformity over a full-scale 4-inch wafer

with a small variation of less than 1%, Figure 2(e). The chemical inertness of SiC electrodes along with high quality and uniform thermal oxide layers enable the formation of a hybrid nanomembrane structure, where SiC functions as a robust bio-electronic interface, and silicon oxide offers a stable biobarrier for long-term implanted, flexible electronics.

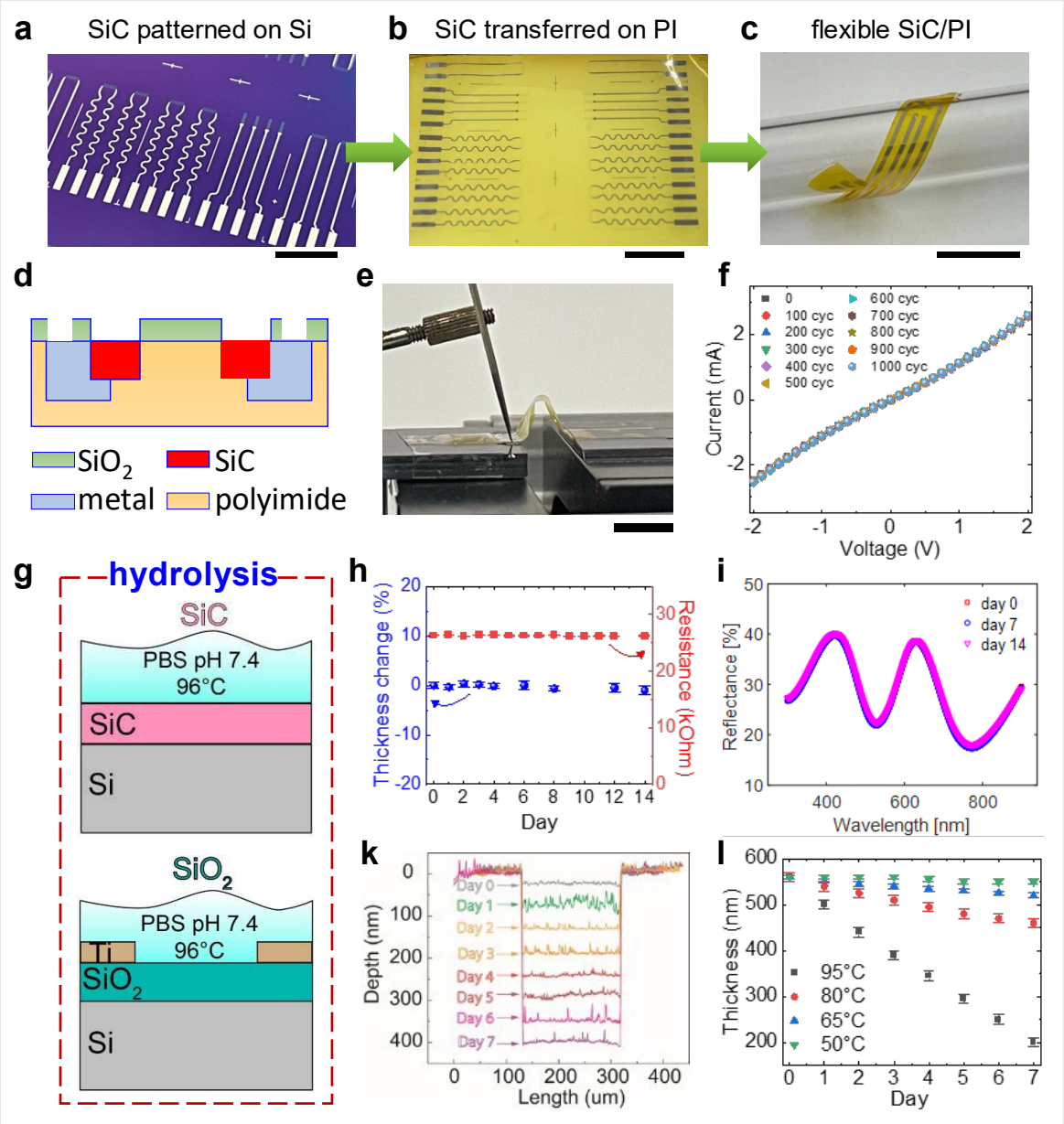


**Figure 3.** Long-term test of SiC/SiO<sub>2</sub> electronics for implanted application: a) Structured SiC and metal on a Si substrate by CMOS processes. b) transferred SiC/metal onto polyimide substrate. c) bendability of SiC on polyimide sample, scale bar, 10 mm. d) cross-sectional view of flexible SiC electronics after SiO<sub>2</sub> passivation and metallization. e) Real-time

electrical measurement during the bending test of flexible SiC on polyimide, scale bar, 10mm. f) Current-voltage characteristics of SiC after 1000 bending cycles. g) Soaking hydrolysis test of SiC and as-grown SiO<sub>2</sub> in PBS 1X at various test temperatures up to 96°C. h) SiC thickness and electrical resistance variations after the accelerated hydrolysis test in PBS at 96°C after up to 14 days. i) Optical reflectance of SiC after soaking in PBS 1X 96°C for 7 and 14 days. k) Depth profiles of SiO<sub>2</sub> in PBS 1X 96°C for up to 7 days. l) thickness changes of SiO<sub>2</sub> in PBS 1X at 96°C, 80°C, 65°C, and 50°C for up to 7 days.

### **Long-term stability of integrated SiC/SiO<sub>2</sub> material system**

Figure 3 (a)-(c) presents optical photographs of SiC/SiO<sub>2</sub> electronics on Si and polyimide substrates, respectively. After transferring SiC/SiO<sub>2</sub> from the original Si substrate onto polyimide, our material system is highly flexible and can be wrapped around the curvilinear surface of a glass cylinder. Figure 3(d) illustrates the cross-sectional layered structure of the SiC/SiO<sub>2</sub> flexible electronic system including active SiC electrodes and sensors, and metal interconnect which were passivated by SiO<sub>2</sub>. All materials were hosted on a 10µm-thick polyimide substrate.

Implanted devices would typically experience continuous bending and folding due to the contraction and expansion of biological tissue. To investigate the mechanical flexibility of SiC/SiO<sub>2</sub>/PI, we applied a multiple cycle buckling test with a bending radius of 3mm using a linear motor (Zaber<sup>TM</sup> X-LHM-E), Figure 3(e). The corresponding strain was estimated to be 0.17% ( $\epsilon = 2t/R$ ), well within the tensile strength of SiC and SiO<sub>2</sub> (i.e., approx. 0.84% and 0.72%)<sup>30,34</sup>, and metallic materials. After 1,000 bending cycles, we did not observe any defect, crack, or delamination occurring on the devices. The current-voltage (I-V) characteristic of the tested devices was also recorded for every 100 bending cycles, showing excellent consistency which further confirms the robustness of the SiC/SiO<sub>2</sub> biointerface and biobarrier under mechanical stimuli, Figure 3(f). This high flexibility is realized due to the small bending

stiffness in nanothin SiC and SiO<sub>2</sub> films as well as the use of the thin polyimide substrate (10µm) which minimizes the distance of the functioning layer to the mechanical neural axis (see the finite element analyses (FEA) simulation result in Supplementary Note 4).

As important as mechanical flexibility, the resilience of the biointerface and biobarrier materials to hydrolysis reaction is another key feature for long-lived implantable electronics. To investigate this property, we soaked SiC and SiO<sub>2</sub> nanomembranes into an *in vitro* bio-simulated electrolyte (i.e., phosphate-buffered saline (PBS 1X) pH=7.4) (see Supplementary Note 5). The hydrolysis experiment was performed at 96°C as a means of accelerating the chemical reaction, in which the lifetime of our material system can be estimated using the Arrhenius extrapolation:  $lifetime \propto \exp(E_a / K_B T)$ , where  $E_a$  is the activation energy (i.e., 1.32 eV for the case of SiO<sub>2</sub>),  $K_B$  is the Boltzmann constant, and  $T$  is the accelerated test temperature<sup>35</sup>. To measure the change in the thickness of SiC and SiO<sub>2</sub> nanomembranes, we sputtered and patterned titanium (Ti) windows with a thickness of 100nm onto these films. As Ti rarely reacts with water molecules even at elevated temperatures, it functions as the hydrolysis mask for the subsequent depth profile measurement. Figure 3(h) plots the thickness and electrical resistance of the SiC films against the testing period (in PBS at 96°C). These two parameters remained almost unchanged over 14 days at 96°C, indicating the superior stability of SiC in the biofluid environment. The stable optical property (i.e., optical reflectance) in the SiC/Si bilayer after being soaked in the PBS solution for up to 14 days suggests the suitability of SiC nanomembranes for implanted optoelectronic applications, Figure 3(i). Compared to SiC, SiO<sub>2</sub> experiences a considerable higher hydrolysis rate, which can be clearly recognized from the depth measurement, Figure 3(k). At 96°C, the SiO<sub>2</sub> thickness changed at a rate of approximately 50nm per day. Lowering the testing temperature from 96°C down to 80°C, 65°C, and 50°C significantly slows down the hydrolysis rate to 11.5nm/day, 2.1nm/day, and 0.4nm/day, respectively. By fitting the hydrolysis rate and testing temperature using an Arrhenius approximation, the lifetime of 580nm SiO<sub>2</sub> at physiological body temperature (37°C)

is estimated to be over 30 years. These results suggest that the SiC/SiO<sub>2</sub> material system can last for several decades, making it highly suitable for long-term implanted biomedical devices. More importantly, as the SiC is almost unaffected by the surrounding extracellular fluid, the lifetime of the device mainly depends on that of the SiO<sub>2</sub> insulation layer, which can be extended by increasing the film thickness. Another promising possibility is a partly biodegradable implanted system, where the dissolution timeframe is defined by the SiO<sub>2</sub> layers, while a minimal amount of biocompatible SiC materials would potentially be allowed to remain inside the human body.

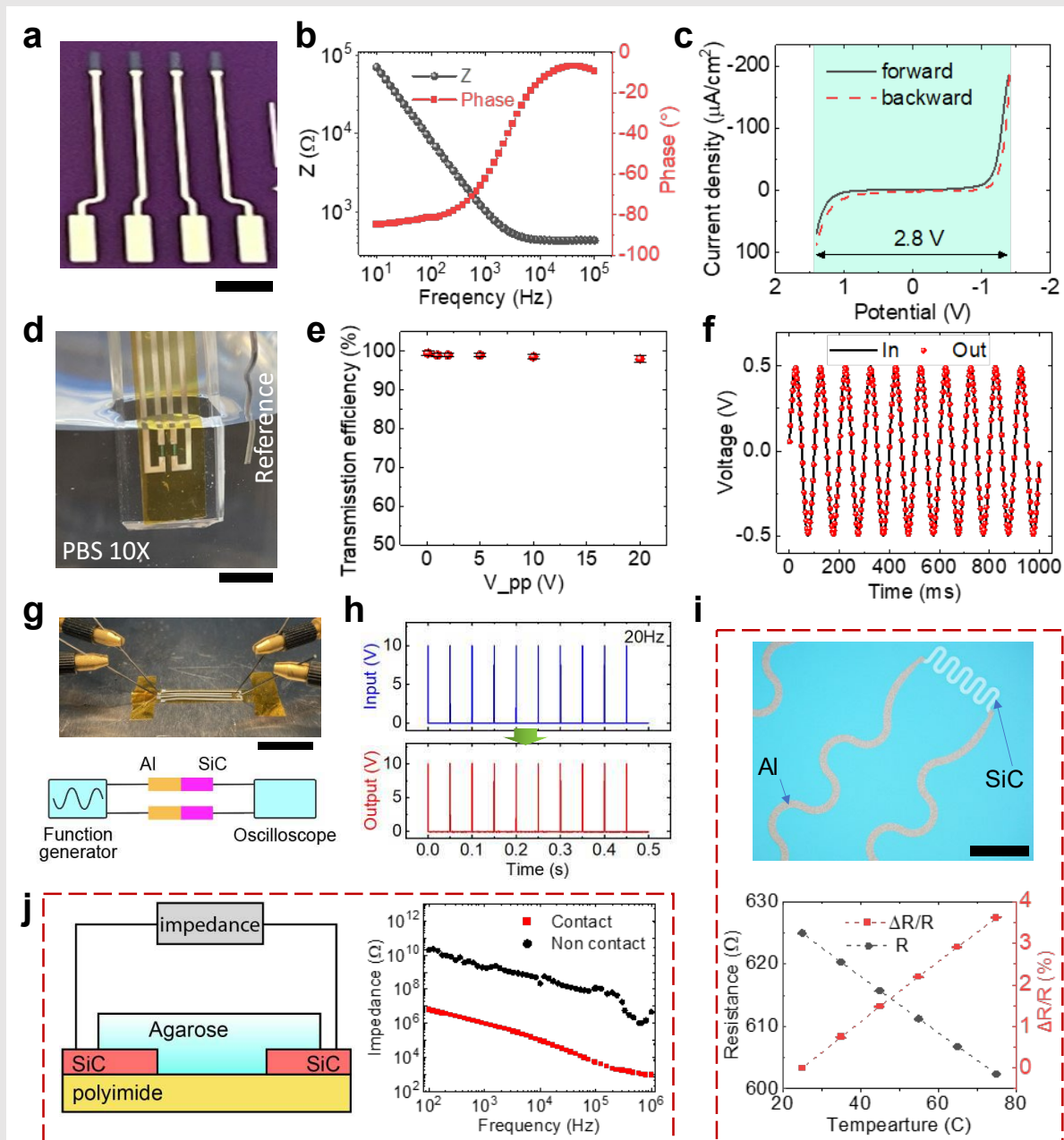


**Figure 4.** Multimodal SiC/SiO<sub>2</sub> bio electrodes and integrated sensors: a) optical photograph of fabricated SiC electrodes incorporated with metal contact, scale bar, 1mm. b) electro impedance spectroscopy (EIS) of single crystal SiC electrodes: impedance and phase angle versus frequency from 100Hz to 1MHz. c) cyclic voltammetry scan of SiC electrode in 0.1 M PBS (pH=7.4) at the scan rate of 0.1 V s<sup>-1</sup>. d) bio simulated measurement with Pt reference electrode in 0.1 M PBS, scale bar, 5mm. e) transmission efficiency of ac electrical stimulation. f) matching output voltage with applied ac signal at 20Hz. Stimulated

monophasic experiment: g) experimental apparatus, scale bar, 10mm. h) comparison between input and output signal. i) demonstration of integrated temperature sensor, scale bar, 500 $\mu$ m. j) contact sensing with hydrogel model using SiC electrode.

### **Multimodal electronics for biointerfacing and sensing**

Figure 4(a) shows an optical image of a SiC bioelectrode array. The electrochemical impedance spectra (EIS) of SiC as active electrodes was characterized in PBS 1X pH 7.4 for a frequency ranging from 10 Hz to 1 MHz, Figure 4(b) using a CH Instruments<sup>TM</sup> CHI 660E. At the starting frequency of 10Hz, SiC electrodes show a relatively high impedance of approximately 80k $\Omega$ . However, the impedance significantly decreased at higher frequencies and then stabilized at frequencies above 6kHz. The interfacial impedance of the SiC electrode at 1kHz was approximately 1k $\Omega$ , well within the typical range of less than 600k $\Omega$  which is viable for physiological applications.<sup>12</sup> The experimental data indicates highly doped SiC as an excellent material for Faradaic interfaces. As important as the EIS, the potential window of the active electrode is a critical factor for neurological stimulation applications. Figure 4(c) shows a cyclic voltammetry (CV) measurement of SiC electrodes in 1X PBS. Accordingly, the SiC electrode possesses a wide potential window of -1.4V to 1.4 V, without any redox peaks in this range. The potential window of 2.8V in our n-doped 3C-SiC is one of the highest electrochemical windows reported, which is larger than that of boron-doped diamond with sp<sup>2</sup> impurity (-0.8 to 1.5V). The advantages of a wide electrochemical window include (i) safety implications for neuron stimulation with the absence of electrochemical reactions of water, and (ii) the capability of detection of analytes across a wide range of electrical potentials without the interference of the background current caused by the reduction/oxidation of water. We calculated the charge storage capacity (CSC) as,  $CSC = \int_{E_c}^{E_a} |i| dE / \nu A$ , where  $i$ (A),  $E$ (V),  $\nu$ (V s<sup>-1</sup>),  $A$ (cm<sup>2</sup>) are output current, applied voltage, scanning rate, and active area of the SiC electrodes, respectively<sup>36</sup>; and the CSC of the SiC electrode was found to be 735 $\mu$ C.cm<sup>-2</sup> (for

an opening area of  $1500\mu\text{m} \times 2000\mu\text{m}$ ) This CSC value is considerably higher than that of other common wide bandgap semiconductors such as diamond boron-doped diamond, indicating the applicability of SiC for implanted neuron stimulation<sup>37</sup>.

Further from the fundamental characterization of SiC electrochemistry, we demonstrated the recording and stimulation function of the SiC electrode in a bio-simulated environment as shown in Figure 4(d)-(f). Here, a sinusoidal signal was generated from a Pt working electrode at different magnitudes ranging from 0.1V to 20V and at a frequency of 10Hz, Figure 4(d). The emitted electrical potential propagated through the biofluid media (i.e., 1X PBS) and was captured by a flexible SiC electrode placed adjacent to the Pt electrode, Figure 4(e). The output voltage recorded by an oscilloscope (i.e., Keysight<sup>TM</sup> MSOX2022A) shows an excellent gain (i.e.,  $V_{\text{out}}/V_{\text{in}}$ ) of approximately 0.98, close to the ideal value of 1, Figure 4(f). We further evaluate the capability of SiC for Faradaic interface using an *in vitro* model illustrated in Figure 4(g), in which stimulated monophasic signals (i.e., 10V amplitude, 20Hz frequency, 1% duty cycle) were generated from a function generator. The output signal was then simultaneously picked up at the flexible SiC terminals, which exhibits a comparable voltage (i.e., 10V) and a similar wave form to the emitted input, Figure 4(h). This closely matched value between the input and output signals is attributed to the electrical continuity of the metal traces along with the low electrical resistance of the highly doped SiC nanomembranes. These *in vitro* studies suggest a promising possibility of using SiC/SiO<sub>2</sub> bioelectronics to underpin *in vivo* biological investigations (e.g., on an animal model).

As well as the Faradaic interface, SiC/SiO<sub>2</sub> electrodes can also be utilized as a multifunctional platform for real-time monitoring of several biophysical parameters, that could serve as a powerful tool for biomedical implanted applications. One of those promising functions is body temperature sensing, utilizing the thermoresistive effect in SiC nanomembranes. Figure 4(j) plots the response of the SiC temperature sensors for a range of 25°C to 80°C. The significant resistance change with varying temperature ( $\Delta R/R \sim -3.6\%$  for

$\Delta T=50^{\circ}\text{C}$ ) indicates that SiC is a good candidate for the development of thermal sensors. The negative temperature coefficient of resistance (TCR) in the n-type SiC was originated from the dominance of thermally activated carrier density over the decrease in electron mobility caused by phonon scattering. Another potential application of the soft SiC platform is impedance sensors that can detect the physical contact between electronics and biotissue. Understanding of the contact of bioimplanted electronics and tissues is critical for physiological recording and stimulation, as well as several biomedical treatments such as radio frequency ablation. The working principle of the SiC touching sensor is based on the impedance change of the SiC electrodes under contact with tissue. Specifically, when a pair of SiC electrodes are in contact with biotissue, an additional conducting path is formed in between, which generally reduces the impedance due to the presence of conductive charges in biomaterials. We demonstrate this function using a phantom tissue formed by an ionic hydrogel, a mixture of 2 wt% agarose gel and 98 wt% 0.1M PBS (see Supplementary Note 6). The contact sensor monitors the electrical impedance measured between two adjacent SiC electrodes, Fig. 2(j)-left. When the phantom tissue was not in contact with the SiC sensor, the impedance is dominated by the oxide capacitance between the two SiC electrodes, hence the measured impedance was in a high range (i.e., above 1 M $\Omega$ ) as measured by a LCR meter (i.e., HP<sup>TM</sup> 4284A). When the phantom tissue makes a conformal contact with the sensor, additional electrical conduction paths are formed (i.e., SiC/tissue/SiC significantly reducing the impedance), Figure 2(j)-right. For a frequency range of 100 Hz to 1 MHz, we observed a clear change in the impedance of SiC sensors when forming a contact with phantom tissue, demonstrating the functionality of SiC for touch sensing applications.

### **Neural stimulation on an animal model**

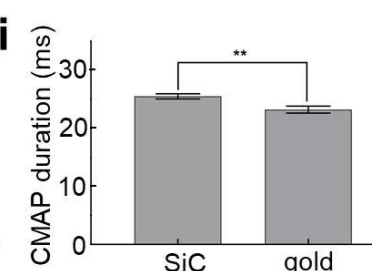
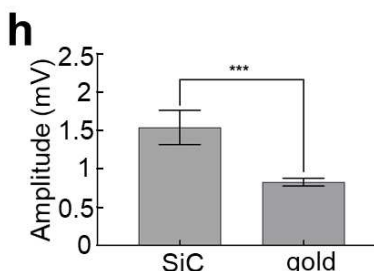
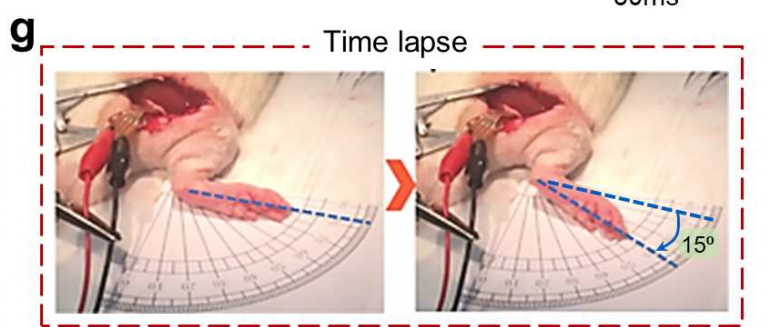
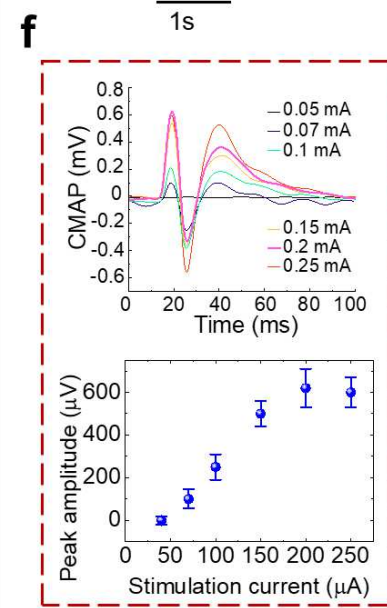
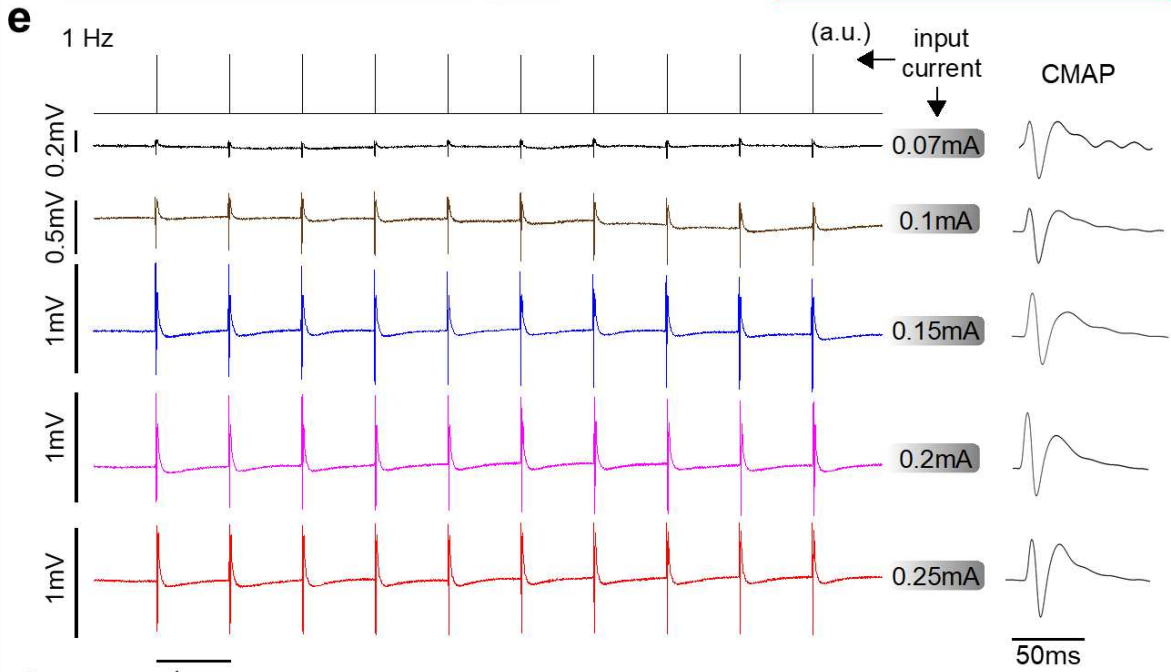
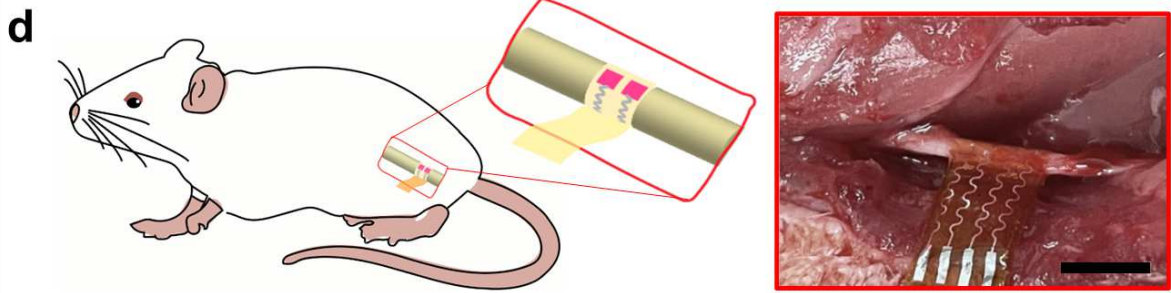
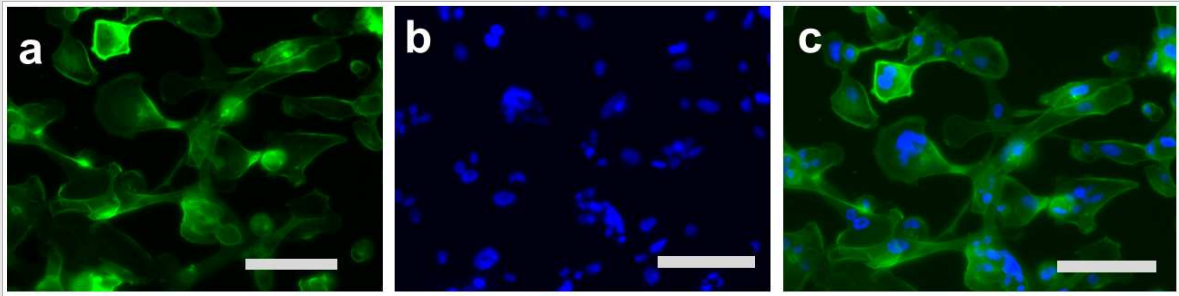


**Figure 5.** Biocompatibility experiment (a-c): The Silicon carbide (SiC) material did not elicit cytotoxicity in human mammary fibroblast (HMF). Fluorescence images: a) actin were stained with green. b) nucleus were stained with blue. (c) merged cells: actin (green) and nucleus (blue) shows the cell attachment and spreading with their general morphology, scale bar, 50 $\mu$ m. Demonstration of in vivo muscle stimulation using implanted SiC electrode (d-i): d) Left: schema of electrical muscle stimulation on a rat sciatic nerve model; Right: photograph of flexible SiC/SiO<sub>2</sub> wrapped around sciatic nerve of a rat scale bar, 5mm. e) Left: recorded CMAP signal from transcutaneous surface electrode with different applied stimulating currents from 0.07 to 0.25 mA using the SiC electrode; Right: CMAP wave forms, not to scale. f) Recorded voltage amplitude at different applied dc currents to SiC stimulation electrodes (Up: overlaying the CMAP response under different stimuli; Down: The relationship between input current and output CMAP). g) Leg movement at the knee joint with a change in angle of >15 degrees. Benchmarking SiC versus standard gold stimulation electrodes: h) amplitude at CMAP supramaximal. i) CMAP duration at supramaximal.

The mechanical characterization and electrochemical analyses suggest flexible SiC/SiO<sub>2</sub> electronics as a potential platform for bioimplanted neuron stimulation. Prior to implanting the electrodes into a rat model, we investigated the biocompatibility of the functioning material (i.e., SiC) using an *in vitro* cell culture approach. Due to its excellent optical transparency, SiC nanomembranes allow for the direct observation of cell growth and proliferation using a standard inverted microscope (see the Method section). Figure 5(a-c) show cell proliferation in SiC electrodes using fluorescent imaging. Evidently, the cell counts on SiC nanomembrane were comparable to that of the controlled sample after five days of growth, while cellular morphology shows the cells appeared to be well attached onto the SiC surface (see

Supplementary Note 7 and Figures S6 & S7). These results demonstrate the biocompatibility of our material system for biological applications.

*In vivo* nerve stimulations were carried out on a rat animal model to demonstrate practical biomedical applications of the soft SiC electronics for neuronal stimulation, Figure 5(d). After exposing the right sciatic nerve located within the gluteal region of the anaesthetized rat (see Method Section and Supplementary Note 8), we wrapped the SiC electrodes around the exposed sciatic nerve. Transcutaneous ring electrodes were secured around the right leg to record the compound motor action potential (CMAP) response from the gastrocnemius muscle. To verify the stimulation effectiveness of the SiC electrode, we compared the CMAP results to that from a commercial bipolar gold electrode (AD instruments) as a reference stimulator (i.e., controlled electrodes) throughout the *in vivo* experiment, Figure S8. The characteristics of the stimulation impulses used for both the SiC and control groups were delivered at 1ms pulse width, with 10 pulses at a frequency of 1Hz. The stimulation current varied between 0.07mA to 0.25mA to assess the response from the muscle by analyzing parameters of peak amplitude and CMAP duration. At stimulus currents below response threshold (e.g., 0.07mA), we did not observe any discernable CMAP response in both groups. Increasing the current intensity resulted in an onset CMAP response (Figure 5e) that increased in amplitude relatively consistent and comparable with the control electrode. At stimulus currents above 0.2mA, the recorded CMAP response reached its supramaximal response and remained constant even when increasing the current intensity. This observation is reasonable as the evoked supramaximal CMAP response is typically the summation of the action potentials generated from all the activated motor axons within the whole sciatic nerve. A low current intensity (<0.07mA) may only excite a small number of axons, which is not recordable with the surface electrodes. Increasing the stimulus current leads to a rise in the number of activated motor axons, resulting in a higher compounded voltage in the innervated muscle (e.g., gastrocnemius). When the stimulus current reached ~0.2 mA (for both the SiC electrode and control), most motor axons were assumed to be activated

due to the CMAP amplitude reaching its supramaximal signal, Figure 5(f). Sufficient stimulus current can be visually observed that generates leg movement at the knee joint angle resulting in  $\sim 15$  degrees displacement, Figure 5(g). The movement of the leg under electrical stimulation suggests a promising possibility of using flexible SiC/SiO<sub>2</sub> implanted electronics to regain limb control in patients with paralysis. It should be noted that at a higher stimulus current -which resulted in the leg movement- the SiC/SiO<sub>2</sub> nanomembranes maintained a good conformal contact with the sciatic nerve, which is reflected by the stable and constant CMAP signal over 10 continuous pulses. The CMAP amplitude and duration at a supramaximal response generated from the SiC electrodes and the control device were extracted from the action potential recording and plotted in Figures 5 (h)(i). CMAP amplitude is a neurophysiological parameter that represents the number of motor axons active during stimulation<sup>38</sup>. In these series of experiments, the SiC electrode displayed a mean amplitude of  $1.54 \pm 0.22$  mV (n=3), while the control (gold electrode) displayed a mean amplitude of  $0.82 \pm 0.05$  mV (n=3). The SiC electrode displayed a significantly higher (p-value 0.0008) amplitude than the control. This difference could be explained by the greater conformal surface area contact between the interface of the SiC electrode and epineurium of the sciatic nerve, resulting in a greater number of active motor axons, thus supplying more muscle fibers, and increasing the CMAP amplitude.

The CMAP duration in neurophysiological studies represents the synchrony of firing of the motor neurons and thus the coordinated active muscle contraction<sup>39, 40</sup>. Our results display a significant difference in duration (ms) between the SiC electrode and the control (p-value 0.0016; n=3). The mean duration of the control was  $23.21 \pm 0.60$  ms, compared with the SiC electrode, which was  $25.49 \pm 0.45$  ms. The difference seen between the two electrodes could be explained simply by the fact that if less axons were activated (as mentioned above) due to the interface contact of the control electrode to the epineurium, then less muscle fibers are required to fire in synchrony. Another plausible explanation for this increase in CMAP duration is the distance between the anode and cathode of the stimulating electrode, which was

considerably shorter in the control compared to the SiC – which wrapped around the entire nerve’s circumference. However, it must be acknowledged that one of the pitfalls of nerve-conduction studies is the movement of the recording electrodes during supramaximal stimulation. This is somewhat unavoidable, particularly when changing between different stimulating electrodes and there is significant limb movement of the animal’s lower extremity. Nonetheless, it is evident that the SiC electrodes are able to successfully stimulate the peripheral nerve comparable to a gold-standard control, as shown in Supplementary Information Figure S8.

### **Conclusion**

The present work introduces an innovative material concept for long-lived implanted electronics using highly doped SiC as a Faradaic interface and thermal oxide as an electrical insulation layer. Our unique fabrication pathway is realized owing to the chemical inertness of epitaxial 3C-SiC nanomembranes which allows for high temperature silicon oxidation without altering the physical and chemical properties of the functioning material (i.e., SiC electrodes). Our experimental results suggest the extremely low hydrolysis in SiC/SiO<sub>2</sub> hybrid structures which enable underlying electronics to last for several decades and potentially over the lifetime of patients to provide desired functions. The mechanical characterization confirmed the flexibility of SiC/SiO<sub>2</sub> on polyimide with small bending angles that can make a conformal contact with biotissue. *In vivo* studies on the animal model validated the feasibility and capability of flexible SiC electrodes for neuron stimulation, which can be clearly observed through the muscle action potentials. We envision that the proposed platform can be integrated with multifunctional components including temperature, strain, and pressure sensors along with bio-amplifiers (e.g., nanomembrane transistor) that can offer a powerful tool for central and peripheral neuromodulation applications.

## Methods

*Material development. SiC growth:* Atomic SiC layers were deposited onto a Si substrate using a hot-wall chamber (i.e., Epiflex) at a temperature of 1250°C. To remove native oxide and organic residuals, the Si substrate was thoroughly cleaned using a standard cleaning procedure (i.e., RCA (Radio Corporation of America) cleaning). The Si surface was first carbonized to facilitate an alternating supply of epitaxy (ASE) cycles of SiH<sub>4</sub> and C<sub>2</sub>H<sub>6</sub> gases to provide Si and C precursors. N-type doped SiC was formed using an in situ doping method using NH<sub>3</sub>. SiC. *SiO<sub>2</sub> passivation:* Wet oxidation process of SiC on Si wafer was performed in a semiconductor type diffusion furnace (i.e., HiTech™ Furnaces UK). Oxidation was sourced from water vapor at 96 °C with a carrier gas (i.e., nitrogen). Water vapor pressure and temperature was precisely controlled though out the wet oxidation at temperature of 900+/-0.5 °C for 10 h.

*Device fabrication.* From as-grown a SiC on Si wafer, the SiC layer was patterned to obtain SiC structures on Si substrate. After the SiC on Si wafer was oxidized, the back side oxide layer was removed by a standard oxide removal procedure. The front side with patterned SiC was deposited with a metal layer then wet etched to form interconnects. Flexible substrate (i.e., polyimide) was spin coated with a thickness of 10µm to ensure the flexibility. The host Si substrate was completely removed by two dry etching steps. Oxide windows were created by standard photolithography and wet oxide etching. Further details are available in the Supplementary Notes 1 & 2 and Figure S1 & S2.

*Electrochemical analysis.* The electrochemical analysis on the prepared SiC membrane was conducted in a CHI 660E electrochemical analyzer (CH Instruments™, USA) using a single compartment cell with 3-electrode configuration with SiC as working electrode, the Pt gauze as counter electrode and reference Ag/AgCl electrode. The redox peaks were analyzed by cyclic voltammetry (CV) under a potential window of ±1.4V (vs. Ag/AgCl) at 100 mV·s<sup>-1</sup>,

while electrochemical impedance spectra (EIS) were performed at open circuit potential (-0.5V). Both analyses were performed under an ambient condition containing 1x PBS as electrolyte.

*Cell culture protocol.* Human mammary fibroblast (HMF) from ATCC were grown and maintained in DMEM/F12 (Gibco, Thermo Fisher Scientific, Waltham, MA, USA) medium with 10% fetal bovine serum (FBS) and 1% penicillin/Streptomycin. The cells were cultured in T75 flasks at 37 °C in a humidified atmosphere with 5% CO<sub>2</sub>. The cells were harvested at 80% confluency. Prior to seeding the cells on the test material for the biocompatibility assay, test material (SiC) was sterilized with 80% ethanol and washed three times with sterile 1 X Hank's balanced salt solution (HBSS) followed by UV radiation for 30 mins. The cells were seeded on the sterile material and were further analyzed for cell morphology and cell proliferation assay.

*In vivo sciatic nerve stimulation.* All the procedure were approved by the Research Information Management System (RIMS) - Animal Research Ethics (Protocol number: ENG/01/21/AEC). A total of 3 adult male Wistar rats aged three months with an average weight 450 g, were used for the experiment. Surgery was performed on the right sciatic nerve. The sensing surface ring electrode (red) was positioned where the gastrocnemius muscle has its maximum diameter. The reference surface ring electrode (black) is placed just beneath the sensing electrode. Contact gel was employed to optimize the conductivity/transfer resistance. A skin incision was performed extending from a midpoint (between the hip joint and ischial tuberosity) to the knee. Blunt dissection was carried out (muscle splitting approach) using Iris scissors between the gluteus maximus and biceps femoris muscle. The sciatic nerve was identified under the gluteus maximus muscles. The nerve was isolated from the surrounding connective tissues and fascia using micro-scissors. The epineurium and its blood vessels were preserved.

## Acknowledgements

The authors acknowledge Prof. John A. Rogers from Northwestern University, IL, USA for his valuable comments and suggestion on long-lived implanted electronics. This work was partially funded by the discovery grant DE200100238 from the Australian Research Council (ARC) and the Griffith IMPACT Spotlight (Integrated Microelectronic Platform for Advanced health-Care). Yusuke Yamauchi acknowledges the support from JST-ERATO (YAMAUCHI Materials Space-Tectonics Project – JPMJER2003), Japan. This work was performed in part at the Queensland node of the Australian National Fabrication Facility. A company established under the National Collaborative Research Infrastructure Strategy to provide nano and microfabrication facilities for Australia’s researchers.

## References

1. Wagner FB, *et al.* Targeted neurotechnology restores walking in humans with spinal cord injury. *Nature* **563**, 65-71 (2018).
2. Pena Pino I, *et al.* Long-Term Spinal Cord Stimulation After Chronic Complete Spinal Cord Injury Enables Volitional Movement in the Absence of Stimulation. *Front Syst Neurosci* **14**, 35 (2020).
3. Behrman AL, Ardolino EM, Harkema SJ. Activity-Based Therapy: From Basic Science to Clinical Application for Recovery After Spinal Cord Injury. *J Neurol Phys Ther* **41 Suppl 3**, S39-S45 (2017).
4. Jones ML, *et al.* Activity-based therapy for recovery of walking in individuals with chronic spinal cord injury: results from a randomized clinical trial. *Arch Phys Med Rehabil* **95**, 2239-2246 e2232 (2014).
5. Someya T, Bao Z, Malliaras GG. The rise of plastic bioelectronics. *Nature* **540**, 379-385 (2016).
6. Rotenberg MY, Tian B. Bioelectronic devices: Long-lived recordings. *Nature Biomedical Engineering* **1**, (2017).
7. Kemp SW, Cederna PS, Midha R. Comparative outcome measures in peripheral regeneration studies. *Exp Neurol* **287**, 348-357 (2017).
8. Koo J, *et al.* Wireless bioresorbable electronic system enables sustained nonpharmacological neuroregenerative therapy. *Nat Med* **24**, 1830-1836 (2018).
9. Ulloa L. The vagus nerve and the nicotinic anti-inflammatory pathway. *Nat Rev Drug Discov* **4**, 673-684 (2005).

10. Xiang Z, *et al.* Progress of Flexible Electronics in Neural Interfacing - A Self-Adaptive Non-Invasive Neural Ribbon Electrode for Small Nerves Recording. *Adv Mater* **28**, 4472-4479 (2016).
11. Song E, *et al.* Flexible electronic/optoelectronic microsystems with scalable designs for chronic biointegration. *Proc Natl Acad Sci USA* **116**, 15398-15406 (2019).
12. Song E, Li J, Won SM, Bai W, Rogers JA. Materials for flexible bioelectronic systems as chronic neural interfaces. *Nat Mater* **19**, 590-603 (2020).
13. Chen R, Canales A, Anikeeva P. Neural Recording and Modulation Technologies. *Nat Rev Mater* **2**, (2017).
14. Jonsson A, *et al.* Therapy using implanted organic bioelectronics. *Sci Adv* **1**, e1500039 (2015).
15. Koo JH, Song J-K, Kim D-H, Son D. Soft Implantable Bioelectronics. *ACS Materials Letters* **3**, 1528-1540 (2021).
16. Normann RA. Technology insight: future neuroprosthetic therapies for disorders of the nervous system. *Nat Clin Pract Neurol* **3**, 444-452 (2007).
17. Zhang Y, *et al.* Climbing-inspired twining electrodes using shape memory for peripheral nerve stimulation and recording. *Sci Adv* **5**, eaaw1066 (2019).
18. Wu H, Gao W, Yin Z. Materials, Devices and Systems of Soft Bioelectronics for Precision Therapy. *Adv Healthc Mater* **6**, (2017).
19. Kang SK, *et al.* Bioresorbable silicon electronic sensors for the brain. *Nature* **530**, 71-76 (2016).
20. Truong TA, *et al.* Engineering Stress in Thin Films: An Innovative Pathway Toward 3D Micro and Nanosystems. *Small*, e2105748 (2021).
21. Hwang SW, *et al.* Dissolution chemistry and biocompatibility of single-crystalline silicon nanomembranes and associated materials for transient electronics. *ACS Nano* **8**, 5843-5851 (2014).
22. Choi YS, *et al.* Stretchable, dynamic covalent polymers for soft, long-lived bioresorbable electronic stimulators designed to facilitate neuromuscular regeneration. *Nat Commun* **11**, 5990 (2020).
23. Li Y, Li N, De Oliveira N, Wang S. Implantable bioelectronics toward long-term stability and sustainability. *Matter* **4**, 1125-1141 (2021).
24. Pham TA, *et al.* A Versatile Sacrificial Layer for Transfer Printing of Wide Bandgap Materials for Implantable and Stretchable Bioelectronics. *Adv Funct Mater* **30**, (2020).
25. Fang H, *et al.* Capacitively Coupled Arrays of Multiplexed Flexible Silicon Transistors for Long-Term Cardiac Electrophysiology. *Nat Biomed Eng* **1**, (2017).

26. Li J, *et al.* Ultrathin, Transferred Layers of Metal Silicide as Faradaic Electrical Interfaces and Biofluid Barriers for Flexible Bioelectronic Implants. *ACS Nano* **13**, 660-670 (2019).
27. Rozman J, Peclin P, Knezevic I, Mirkovic T, Gersak B, Podbregar M. Heart function influenced by selective mid-cervical left vagus nerve stimulation in a human case study. *Hypertens Res* **32**, 1041-1043 (2009).
28. Neuser MP, Teckentrup V, Kuhnel A, Hallschmid M, Walter M, Kroemer NB. Vagus nerve stimulation boosts the drive to work for rewards. *Nat Commun* **11**, 3555 (2020).
29. Mridha Z, *et al.* Graded recruitment of pupil-linked neuromodulation by parametric stimulation of the vagus nerve. *Nat Commun* **12**, 1539 (2021).
30. Nguyen TK, *et al.* Superior Robust Ultrathin Single-Crystalline Silicon Carbide Membrane as a Versatile Platform for Biological Applications. *ACS Appl Mater Interfaces* **9**, 41641-41647 (2017).
31. Nguyen T, *et al.* Giant piezoresistive effect by optoelectronic coupling in a heterojunction. *Nat Commun* **10**, 4139 (2019).
32. Phan HP, *et al.* Long-Lived, Transferred Crystalline Silicon Carbide Nanomembranes for Implantable Flexible Electronics. *ACS Nano* **13**, 11572-11581 (2019).
33. Pasquarello A, Hybertsen MS, Car R. Interface structure between silicon and its oxide by first-principles molecular dynamics. *Nature* **396**, 58-60 (1998).
34. Sharpe WN, Pulskamp J, Gianola DS, Eberl C, Polcawich RG, Thompson RJ. Strain Measurements of Silicon Dioxide Microspecimens by Digital Imaging Processing. *Experimental Mechanics* **47**, 649-658 (2007).
35. Fang H, *et al.* Ultrathin, transferred layers of thermally grown silicon dioxide as biofluid barriers for biointegrated flexible electronic systems. *Proc Natl Acad Sci USA* **113**, 11682-11687 (2016).
36. Kim HS, *et al.* Oxygen vacancies enhance pseudocapacitive charge storage properties of MoO<sub>3-x</sub>. *Nat Mater* **16**, 454-460 (2017).
37. Garrett DJ, Tong W, Simpson DA, Meffin H. Diamond for neural interfacing: A review. *Carbon* **102**, 437-454 (2016).
38. Anderson MA, *et al.* Astrocyte scar formation aids central nervous system axon regeneration. *Nature* **532**, 195-200 (2016).
39. Mallik A, Weir AI. Nerve conduction studies: essentials and pitfalls in practice. *J Neurol Neurosurg Psychiatry* **76 Suppl 2**, ii23-31 (2005).
40. Lee S, *et al.* Selective stimulation and neural recording on peripheral nerves using flexible split ring electrodes. *Sensors and Actuators B: Chemical* **242**, 1165-1170 (2017).

## Supplementary Files

This is a list of supplementary files associated with this preprint. Click to download.

- [Supplementaryinformation.docx](#)